PHOTONICS Research

Visible-frequency nonvolatile reconfigurable Janus metasurfaces for dual-wavelength-switched and spin-asymmetric holograms

Huan Yuan,[1] Zheqiang Zhong,[1,2] and Bin Zhang[1,2,*]

[1]College of Electronics and Information Engineering, Sichuan University, Chengdu 610064, China
[2]Big Data Analysis and Fusion Application Technology Engineering Laboratory of Sichuan Province, Chengdu 610065, China
*Corresponding author: zhangbinff@sohu.com

Received 16 October 2023; revised 21 November 2023; accepted 27 November 2023; posted 28 November 2023 (Doc. ID 509544); published 1 February 2024

Janus metasurface holography with asymmetric transmission characteristics provides new degrees of freedom for multiplexing technologies. However, earlier metasurfaces with asymmetrical transmission faced limitations in terms of tunability and multifunctionality. In this study, we propose a metasurface color holographic encryption scheme with dynamic switching and asymmetric transmission at visible frequencies using a low-loss nonvolatile optical phase-change material, Sb_2S_3. Using a modified holographic optimization strategy, we achieved high-fidelity asymmetric holographic imaging of a nanostructured metasurface. By controlling the incident direction and wavelength of visible light, as well as the level of crystallization of Sb_2S_3, this reconfigurable metasurface enables the precise manipulation of tunable color holographic image displays. In particular, in the semi-crystalline state of Sb_2S_3, the encoded information can be securely encrypted using a two-channel color-holographic image, whereas only a preset camouflaged image is displayed in the crystalline or amorphous state of Sb_2S_3. The proposed multiencrypted Janus metasurface provides a potential approach for dynamic holographic displays with ultrahigh capacity, holographic encryption, and information storage.

https://doi.org/10.1364/PRJ.509544

1. INTRODUCTION

In recent years, metasurfaces have garnered significant attention owing to their flexible manipulation of light and remarkable properties such as being ultralightweight and ultrathin [1–5]. Metasurfaces comprising artificially designed subwavelength units can provide a new paradigm for designing various ultracompact optical components. Owing to rapid advancements in micro-nano manufacturing and computer technologies, metasurfaces have been applied in various miniaturized optical fields, including holographic displays [6–9], optical encryption [10–15], nanoprinting [16–20], edge detection [21,22], diffraction neural networks [23,24], and optical stealth [25]. Deng *et al.* combined the PB and detour phases to design a metasurface with multiple degrees of freedom to achieve a full-color complex amplitude vector hologram [26]. Ni *et al.* developed a multidimensional light-field encoder based on a tunable metasurface that enables the simultaneous measurement of the polarization and spectrum of near-infrared light [27]. However, most of the aforementioned metasurface-based optical elements exhibit symmetric transmission characteristics, where both ends of the metasurface perform the same operation under identical incident conditions [Fig. 1(a)]. Using a focusing lens as an example, the focal length of the incident light is compared along the forward/backward propagation direction. Although this is beneficial for certain applications, it limits the potential for designing advanced multichannel and multifunctional components. With increasing demand for compact and versatile optical components in various fields, it is crucial to break the symmetrical transmission of metasurfaces for a wide range of photon applications.

A crucial property of electromagnetic waves, propagation direction, is often overlooked in comparison to commonly used parameters such as polarization, phase, incident angle, and wavelength. The Janus metasurface, which serves as a research platform for studying optical phenomena such as nonreciprocal transmission, can control the electromagnetic wavefront on both sides, enabling asymmetric reflection/transmission control [Fig. 1(b)] [28,29]. This metasurface has the potential to be a substitute for engineered multifunctional devices such as asymmetric metals and beam shaping [30,31]. However, traditional Janus metasurfaces rely heavily on complex multihierarchical structures, making them difficult to manufacture and expensive. To address these issues, single-layer metasurface structures based on both the propagation and geometric phases have been developed and utilized for asymmetric transmission [32–35].

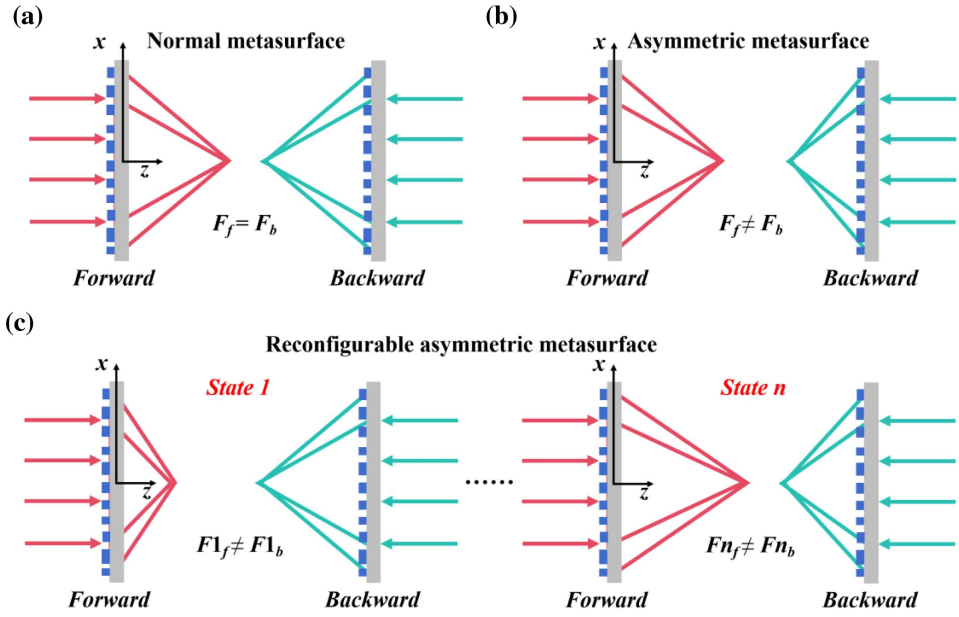

Fig. 1. Schematic comparison of the optical functions of various types of metasurfaces. (a) Schematic diagram illustrating the transmission characteristics on both sides of a traditional transmissive metasurface ($F_f = F_b$). (b) Schematic diagram illustrating the transmission characteristics on both sides of an asymmetric Janus metasurface ($F_f \neq F_b$). (c) Schematic diagram illustrating the transmission characteristics on both sides of a reconfigurable asymmetric Janus metasurface.

For instance, Naveed *et al.* proposed a metasurface comprising hydrogenated amorphous silicon (a-Si:H) and demonstrated asymmetric light transmission in the visible region. Wan *et al.* designed an asymmetric bidirectional metasurface to achieve a wideband bidirectional holographic display. However, the electromagnetic functions of the previously proposed asymmetrically transmitted metasurfaces are statically regulated, limiting their capacity for further expansion.

Fortunately, optical phase-change materials (O-PCMs) are highly desirable for designing tunable optical components owing to their reconfigurable properties [36–42]. O-PCMs typically exist in two primary states, crystalline and amorphous (insulated or metallic). The conversion between these two crystallinity states alters the arrangement of chemical bonds in the material, causing significant changes in its complex refractive index [43]. This enables the introduction of substantial phase and amplitude modulation in compact micro and nano sizes. The crystallinity of the O-PCMs can be altered by applying an external stimulus (such as light, electricity, or heat) [38,44,45], and the reversible switching between two stable states has a high durability of up to 10^{12} cycles [46]. However, classic O-PCMs such as $Ge_xSb_yTe_z$ alloys and VO_2 exhibit high absorption losses at different crystallinity levels and cannot satisfy the requirements for high performance. Additionally, the volatility of VO_2 limits its feasibility in the design of high-performance nonvolatile reconfigurable devices. For instance, Chen *et al.* proposed a terahertz Janus metasurface based on an array of O-PCMs, VO_2, which can achieve asymmetric transport switching [Fig. 1(c)] [47]. When the O-PCMs are in different states, the transmission characteristics of the incident light along the forward and backward propagation directions vary ($F1_f \neq F1_b, \ldots, Fn_f \neq Fn_b$). However, this structure has a complex multihierarchical structure and suffers from the drawbacks of volatile regulation. Furthermore, these metasurfaces can achieve asymmetric transmission only at specific wavelengths and cannot simultaneously regulate different wavelengths, resulting in limited optical possibilities. Recently, two novel antimony-based nonvolatile O-PCMs, Sb_2S_3 (Fig. 2) and Sb_2Se_3, were reported to exhibit significantly low absorption losses at different crystallinity levels [38]. In particular, Sb_2S_3 exhibits low absorption loss in the visible band, enabling the design of devices with adjustable color display functions. For instance, Hemmatyar *et al.* used Sb_2S_3 to fabricate dynamic metapixels that were switchable, highly saturated, efficient, and of high resolution [46]. Therefore, we explored the strategy of using a simple structure, a nonvolatile Janus metasurface based on Sb_2S_3 with multiple degrees of freedom, to achieve dynamically switched asymmetric color holographic displays.

In this study, we propose a novel nonvolatile reconfigurable single-layer Janus metasurface to achieve asymmetric wavefront generation and dynamically switched bidirectional holography. The Janus metasurface utilizes the reconfigurability of the nonvolatile O-PCM Sb_2S_3 and the incident direction dependence. To design switchable asymmetric holograms on single-sized nanostructured metasurfaces, we developed a modified Gerchberg–Saxton (GS) algorithm by considering both the wavelength channels and propagation directions as the design objectives. In comparison with previous complex multilayer cascade designs, this reconfigurable metasurface can integrate multiple functions into a single phase-change element without introducing any additional loss, providing greater flexibility for regulating the light field. By changing the crystallinity of Sb_2S_3, these functions can be actively switched. In this study, we demonstrated a bidirectional asymmetric color-holographic display

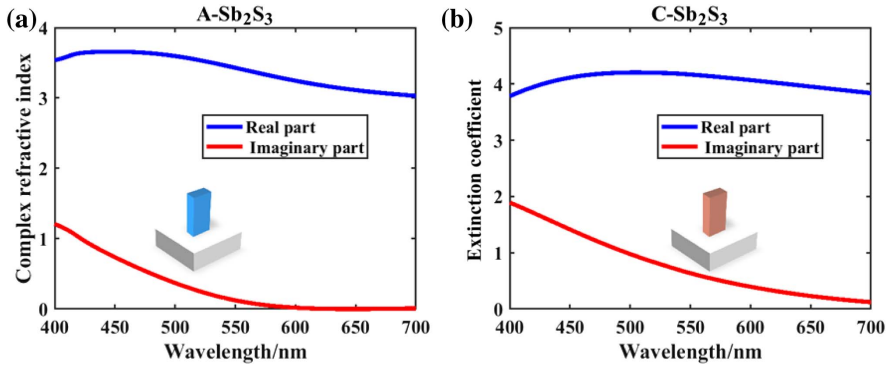

Fig. 2. Complex refractive indices, n, and the extinction coefficients, k, of A-Sb_2S_3 and C-Sb_2S_3 from 400 to 700 nm.

at three different crystallization levels. This scheme not only addresses the limitation of statically switching asymmetric holograms but also achieves multifunction integration on an ultrathin single-size nanostructure, significantly reducing manufacturing complexity and cost. The proposed scheme provides a versatile platform for information multiplexing and is promising for various practical applications, including mass data storage and optical encryption.

2. DESIGN AND METHODS

Figure 3(a) illustrates the concept of a switchable asymmetric hologram based on a nonvolatile reconfigurable Janus metasurface. The scheme allows for the integration of four independent holographic images onto a single metasurface. In the amorphous state, left-circularly polarized (LCP) light is incident forward and backward onto the metasurface, generating green hologram images of a portion of the "lion dance" and a portion of the "dragon" structure in the far field, respectively. In the crystalline state, red hologram images of another portion of the "lion dance" and "dragon" structures are generated in the far field, respectively. In the semi-crystalline state, LCP light is incident forward and backward onto the metasurface, generating complete color holographic images of the "lion dance" and "dragon" structures in the far field. The Sb_2S_3 array, acting as meta-atoms on the metasurface, serves as a half-wave plate to convert circularly polarized (CP) light and enables asymmetric transmission of circularly polarized light. By utilizing the modified GS algorithm, the desired target function can be achieved by calculating the phase distribution on both sides of the metasurface and further arranging the orientation angles of the meta-atoms. Here, a single-phase profile of the meta-atoms array serves as the phase contribution function, encompassing the information required for different wavelength channels and transmission directions. The metasurface can switch between different functions by reversibly changing its crystalline and amorphous states as needed. Figure 3(b) illustrates the decoding keys required for decoding a holographic image and the associated optical properties for various key combinations.

To encode four different hologram images in the far field, we have developed a modified GS algorithm to determine the orientation angle of each meta-atom, as shown in Fig. 4. It is important to note that our geometric phase manipulation technique arises from the inherent property of the meta-atom, which provides two opposite phase distributions for both forward and backward incident CP light. Leveraging this property, we encode the desired phase onto the metasurface and reconstruct two different holographic images simply by changing the direction of incident light. Therefore, the design process of a multifunctional metasurface based on the modified GS algorithm can be divided into three steps [Fig. 4(a)]. (1) Using the GS algorithm, we design the phase required for forward image 1 and backward image 1 at the wavelength of 550 nm. The total geometric phase profile required is then calculated based on the phase merging formula. (2) Similarly, the GS algorithm is used to design the phase required for forward image 2 and backward image 2 at the wavelength of 650 nm. The total geometric phase profile required is then calculated based on the phase merging formula. When two beams of the same CP light are incident from opposite directions, the total geometric phase profile can be expressed as follows:

$$\varphi_{550/650} = \arg[\exp(i\varphi_{\text{forward}}) + \exp(-i\varphi_{\text{backward}})], \quad (1)$$

where φ_{forward} and $\varphi_{\text{backward}}$ represent the geometrical phases required for forward incidence and backward incidence, respectively. The complete phase profile at wavelengths of 550 nm and 650 nm can be obtained by solving Eq. (1), respectively. (3) The required phase exhibits the same profile under two different crystallinity conditions. To integrate the phase profiles corresponding to both states, we develop a formula for merging phases to obtain the final geometric phase, i.e.,

$$\varphi_t = \arg[\exp(i\varphi_{550}) + \exp(i\varphi_{650})], \quad (2)$$

where φ_{550} and φ_{650} represent the geometrical phases required for the amorphous and crystalline states, respectively. In Fig. 4(a), the right side provides a closer look and an overall view of the resulting phase delay distribution when LCP light is incident on the metasurface from either the forward or backward direction. The selection of the meta-atom array is then determined under the principle that the orientation angle of the meta-atom is twice the phase, allowing us to achieve the desired metasurface structure according to the specific requirements.

The specific flow chart of this modified algorithm is depicted in Fig. 4(b). The intensity distributions of the four

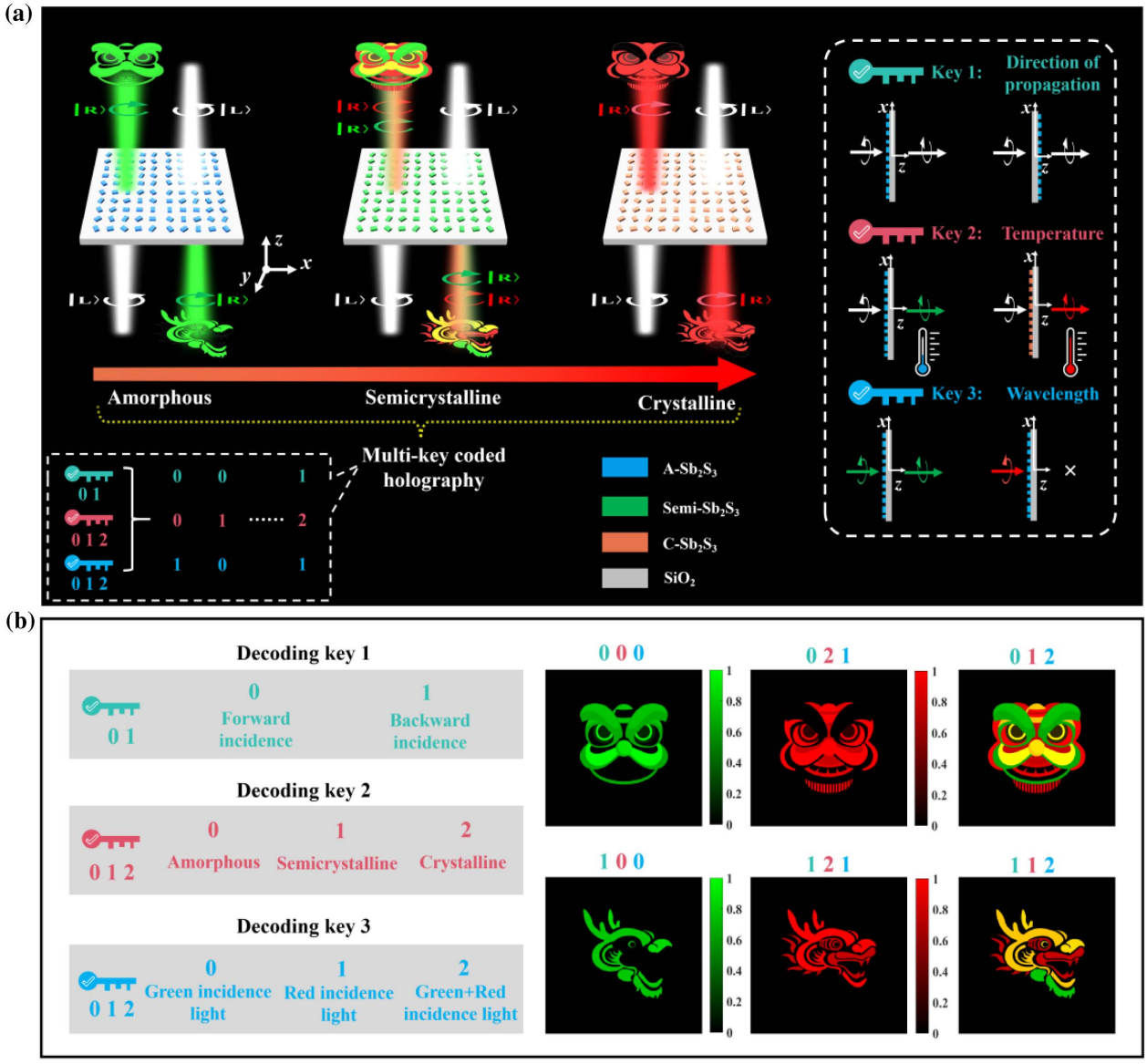

Fig. 3. Scheme for switching an asymmetric hologram based on a nonvolatile reconfigurable Janus metasurface. When LCP white light is incident onto the metasurface, either in a forward or backward direction, four independent holographic images are reconstructed under different states. (b) Left, three different optical decoding keys; right, optical characterization of the nonvolatile reconfigurable Janus metasurface.

images are denoted as A_1, A_2, A_3, and A_4, respectively. The propagation process between the metasurface plane and the target plane is constructed using forward Fresnel diffraction (FFrD) and inverse Fresnel (IFrD) diffraction. The modified GS algorithm differs from the traditional one in that it considers both positive and negative values of the initial random phase before performing the Fresnel diffraction calculation. During the iterative process, the phase enhancement calculation is carried out according to Eqs. (1) and (2), simultaneously fulfilling the requirements of four-channel holographic images. After sufficient iterations, the optimized phase contours $\varphi_{t\_\mathrm{forward}}$ and $\varphi_{t\_\mathrm{backward}}$ are obtained. The distance between the metasurface and the two target planes is set as $z_1 = D_1 = 150$ μm and $z_2 = -D_2 = -150$ μm, respectively. The propagation formulas for both FFrD and IFrD can be expressed as

$$H_z(x,y) = \frac{\exp(ikz)}{ikz}\exp\left[i\frac{k}{2z}(x^2+y^2)\right] \times \mathrm{FFT}\left\{H_0(x_0,y_0)\times\exp\left[i\frac{k}{2z}(x_0^2+y_0^2)\right]\right\}, \quad (3)$$

$$H_0'(x_0,y_0) = \frac{\exp(ikz)}{ikz}\exp\left[i\frac{k}{2z}(x_0^2+y_0^2)\right] \times \mathrm{FFT}\left\{H_z^*(x,y)\times\exp\left[i\frac{k}{2z}(x^2+y^2)\right]\right\}, \quad (4)$$

where $*$ represents complex conjugation, $H_0(x_0,y_0)$ denotes the input light field, and $H_z(x,y)$ is the complex amplitude distribution at the propagation distance z on the observation screen.

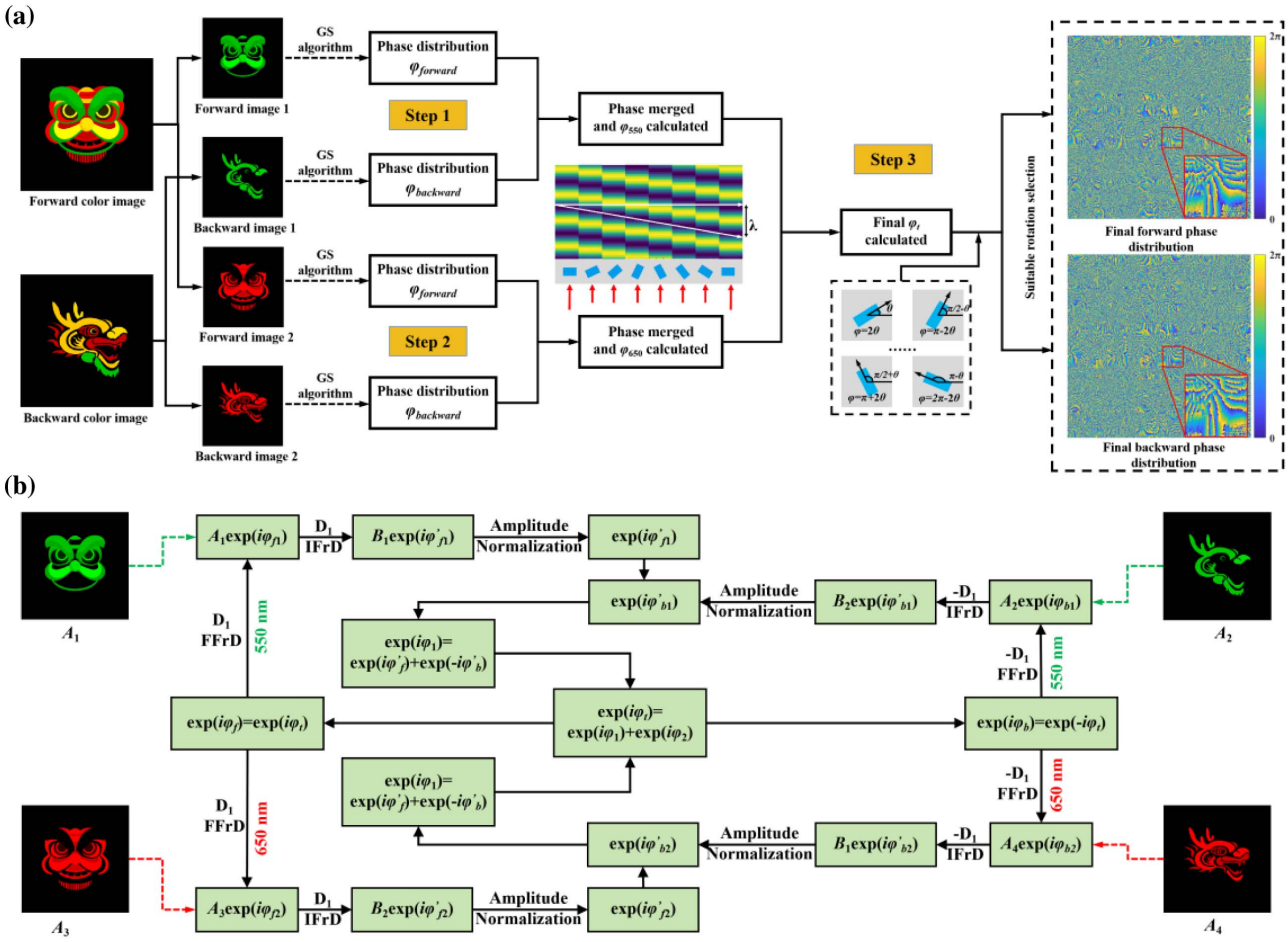

Fig. 4. (a) Detailed flow chart of the reconfigurable asymmetric transmission metasurface design. (b) Optimization process using the modified GS algorithm.

To achieve this desired versatility, we have developed a novel single-layer metasurface structure that breaks symmetrical transmission. By optimizing the structural parameters of the meta-atom, we aimed to meet multiple requirements: (1) the spectral responses of meta-atoms should generate distinct colors in different states; (2) the transmission cross talk between different color channels should be minimized to prevent holographic image cross talk; (3) the circular polarization conversion efficiency should be maximized to ensure clear holographic images. To fulfill these requirements, we employed the particle swarm optimization (PSO) algorithm to optimize Sb_2S_3 square nanorods. Here, we have taken 550 nm (green light) and 650 nm (red light) as the typical examples for the target wavelengths. Therefore, the target spectrum should exhibit narrowband filtering at both target wavelengths and a higher polarization conversion efficiency. The cell period of the elementary meta-atom is fixed at 380 nm ($P = 380$ nm), as shown in Fig. 5(a). The optimized structural parameters include length L, width W, and height H of the meta-atoms. It is worth noting that most O-PCMs have a high extinction coefficient in the visible region, which greatly limits their optical transmission efficiency. In our design, we utilize the nonvolatile O-PCM, Sb_2S_3, as the nanorods and optimize the structure size accordingly. The energy loss is effectively avoided in the visible region due to its low extinction coefficient (the complex refractive index at 633 nm: A-Sb_2S_3, $3.148 + 0i$; C-Sb_2S_3, $3.989 + 0.276i$ for visible light) (Fig. 2). The PSO algorithm yields the optimized structure parameters: $L = 115$ nm, $W = 80$ nm, and $H = 500$ nm. Fortunately, these parameters are compatible with current advanced micro and nano machining technology. The transmission efficiency of the structure is simulated using the commercial software Lumerical finite-difference time-domain (FDTD) solutions. The intensity transmission curve for a single meta-atom under periodic boundary conditions is depicted in Fig. 5(b). The transmission spectrum of incident light can meet the functional requirements mentioned above when Sb_2S_3 is in either its crystalline or amorphous state. Notably, both states exhibit distinct transmission peaks for LCP light at 550 nm and 650 nm, with peak polarization conversion efficiencies of 28.8% and 15.1%, respectively. Additionally, the cross-talk values for the two target wavelength channels are 0.65% and 1.03%, respectively. The cross talk between the two target wavelength channels is negligible. It is worth noting that the peak polarization conversion efficiency at a wavelength of 550 nm is higher than that at 660 nm, due to the lower extinction coefficient of A-Sb_2S_3

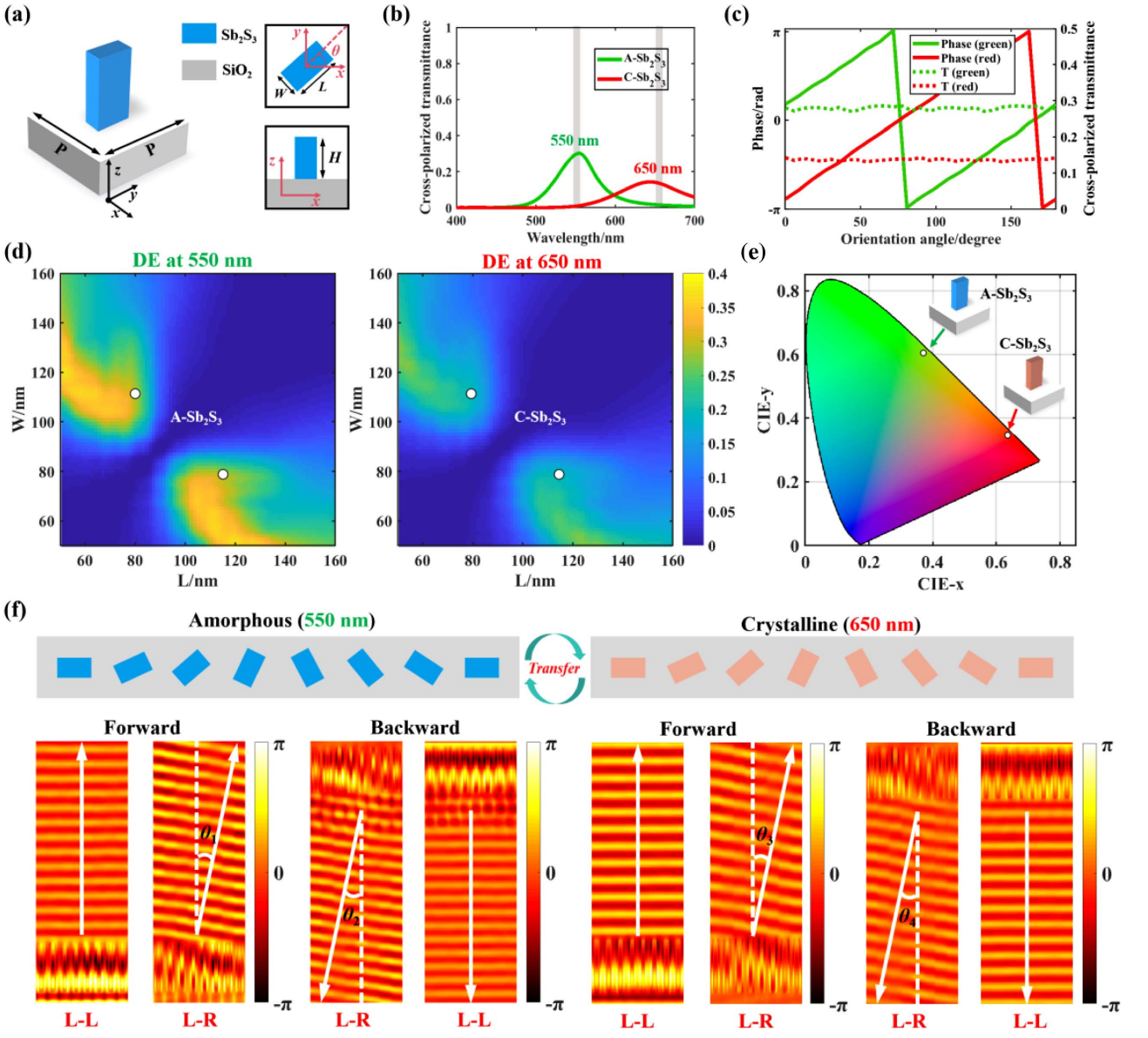

Fig. 5. Structural design and optical properties of meta-atoms. (a) 3D view, side view, and top view of the meta-atom. (b) The transmissivity spectra of cross-polarization conversion are simulated at different levels of crystallization. (c) Cross-polarization transmission and phase variation are simulated at different crystallization levels with varying orientation angles. (d) The function of DE with L and W at the corresponding wavelengths is given for different levels of crystallization. (e) The structural colors in the CIE 1931 chromaticity diagram were calculated by simulating the response of transmission spectra at different levels of crystallization. (f) The beam deflection and deflection angle of LCP light are simulated for both forward and backward incidences.

compared to that of C-Sb_2S_3 (see Fig. 2). To satisfy the required hologram phase, the PB phase principle is adopted to further select the orientation angle of the meta-atoms, assuming the identical sizes of the meta-atoms. The influence of the meta-atom's orientation angle on the polarization conversion efficiency and PB phase in two states is shown in Fig. 5(c). The polarization conversion efficiency remains almost constant at the two target wavelengths, while the PB phase varies twice with the orientation angle ($\varphi = 2\theta$). Thus, the designed structure can meet the target function of the meta-atoms. The diffraction efficiency (DE), defined as the energy ratio between the transmitted and incident beam, is presented in Fig. 5(d) for various structural dimensions L and W, with a thickness of 500 nm. The spectral responses of cross-polarization transmittance in both states are converted into CIE 1931 color space chromaticity plots to quantitatively evaluate the obtained structural colors, as depicted by white solid dots in Fig. 5(e).

In Fig. 5(f), we utilized FDTD solutions to perform numerical calculations to demonstrate the independence of this meta-atom in two different states. By deliberately arranging a periodic array of meta-atoms with varying orientation angles, we intentionally create a complete 2π gradient phase along the interface. This arrangement enables us to prove the abnormal refraction that occurs when two identical light beams are

incident on the metasurface from the opposite sides. As shown in Fig. 5(f), in both states, when the same incident circularly-polarized light is incident on the metasurface from both sides, the outgoing light exhibits opposite beam steering phenomena. Consequently, the wavefronts of the incident light in both forward and backward directions confirm the desired asymmetric transmission performance.

Next, we employed this reconfigurable meta-atom to design a switchable Janus metasurface capable of generating direction-dependent, wavelength-dependent, and crystallinity-dependent holographic images in four channels. To achieve four independent holographic image channels on the metasurface, we utilized the meta-atoms as half-wave plates and rotated the orientation angle of meta-atoms by using geometric phase. Figure 6(a) provides an overview of the metasurface configuration, including top, zoomed, and angled views. The entire metasurface has a size of 38 μm × 38 μm, and it consists of a total of 100 × 100 meta-atoms. Figure 6(b) depicts the flow diagram of the reconstructed image using LCP light of different wavelengths. When Sb_2S_3 is in the amorphous state, both forward and backward incident LCP green light passes through the metasurface, resulting in different encrypted images in the far field. Similarly, when Sb_2S_3 is in the crystalline state, both forward and backward incident LCP red light passes through the metasurface, displaying different encrypted images in the far field. Lastly, when Sb_2S_3 is in the semi-crystalline state, both green and red light, from the same forward and backward incidence, passes through the metasurface, generating different encrypted images with different colors in the far field. The reconfigurable Janus metasurface boasts a high level of encryption and exclusively retrieves the corresponding effective holographic image through the incidence of CP light. When using

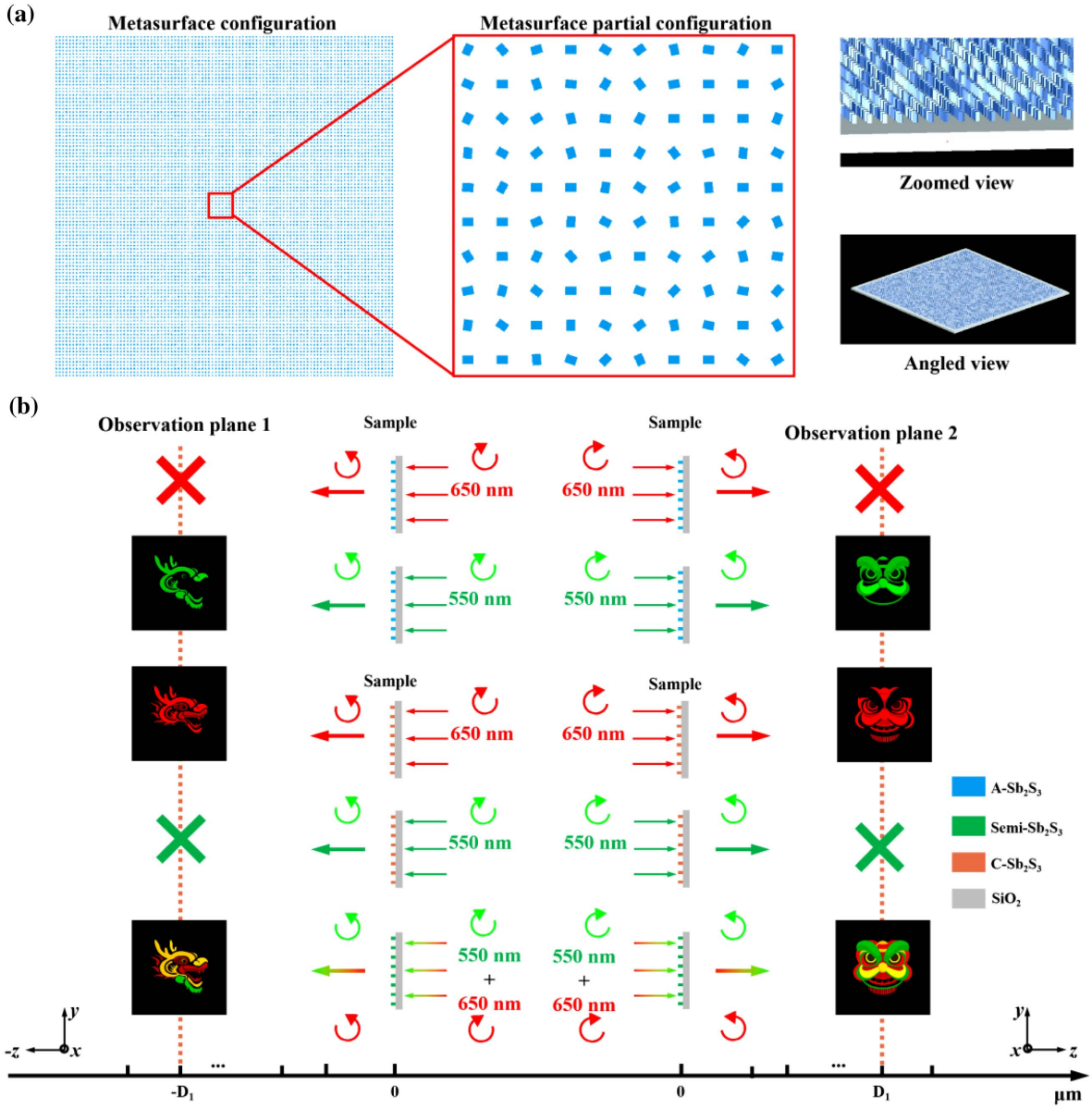

Fig. 6. (a) Diagram of the entire reconfigurable asymmetrical transmission metasurface configuration with top view, zoomed view, and angled view. (b) The flow chart of the image is reconstructed using different wavelengths of LCP light at various levels of crystallinity.

other types of light, such as linearly polarized light, only disordered and invalid image information can be observed. Furthermore, we calculated the broadband transmittance curve of the entire reconfigurable Janus metasurface. Figures 7(a) and 7(b) depict the transmission curves of the metasurface transmission terminal under different crystallinity conditions. The total cross-polarization transmission efficiency at 550 nm in the amorphous state reaches 26.3%, while the corresponding value at 650 nm in the amorphous state reaches 13.5%. Notably, the metasurface exhibits robust transmission performance when utilized for bidirectional dynamic holographic display.

The metasurface enables multichannel image encryption by encoding the incident direction, crystallinity, and wavelength. Figure 8 illustrates the decoding process using different optical keys. The holographic images on the left side of Figs. 8(a) and 8(d) are obtained through numerical calculations using the modified GS algorithm, with each cell containing a total of 800 × 800 pixels. These images exhibit high-fidelity quality in different channels. Additionally, we employed the commercial software FDTD solutions to simulate the metasurface. Due to limited computation resources, the number of pixels was reduced to 100 × 100. The simulation results on the right side of Figs. 8(a) and 8(d) align with the predetermined dynamic multifunction design. The images encoded in different holographic channels are associated with the three optical keys mentioned above and can only be decoded using a specific combination of encoding. This novel holographic encryption scheme can significantly enhance information security and holds great potential for optical encryption application. Moreover, Sb_2S_3 exhibits changes in multiple energy states during its transition from the amorphous state to the crystalline state, allowing the phase transition metasurface to be controlled by a multilevel wavefront. The dielectric constant of the intermediate phases of Sb_2S_3 can be calculated using the Lorenz–Lorentz relation [48]:

$$\frac{\varepsilon_{\text{eff}}-1}{\varepsilon_{\text{eff}}+2}=m\frac{\varepsilon_{\text{C-Sb}_2\text{S}_3}-1}{\varepsilon_{\text{C-Sb}_2\text{S}_3}+2}+(1-m)\frac{\varepsilon_{\text{A-Sb}_2\text{S}_3}-1}{\varepsilon_{\text{A-Sb}_2\text{S}_3}+2}, \quad (5)$$

where m denotes the crystallinity of Sb_2S_3, and $m=0$ and $m=1$ represent the amorphous and crystalline states, respectively. $\varepsilon_{\text{A-Sb}_2\text{S}_3}$ and $\varepsilon_{\text{C-Sb}_2\text{S}_3}$ represent the wavelength-dependent dielectric constants of A-Sb_2S_3 and C-Sb_2S_3, respectively. Figure 8(b) shows the complex refractive index curve for semi-crystalline Sb_2S_3 with $m=0.5$. Taking the wavelength of 633 nm as an example, the complex refractive index of Sb_2S_3 is $3.51+0.10i$. Additionally, we calculated the transmission spectra of meta-atoms in the semi-crystalline state, as depicted in Fig. 8(c). The meta-atoms in the semi-crystalline state exhibit certain transmission efficiency at wavelengths of 550 nm and 650 nm. By simultaneously illuminating the metasurface with red and green light, a new color image can be displayed at both ends. The color lion dance image and color dragon image are displayed respectively at the far field on both sides of the metasurface, as shown in Fig. 8(d). This unique feature enables the presentation of different holographic images in amorphous, semi-crystalline, and crystalline states, thereby expanding the number of channels and enhancing the level of information encryption. It is worth noting that the maximum number of colors that the reconfigurable Janus metasurface can contain depends on two aspects: (1) the number of narrowband filtering channels varying with the crystallinity of Sb_2S_3 nanorods, and (2) the number of hologram wavelength channels optimized using the GS algorithm. Therefore, the maximum number of color channels in the design scheme can be further increased by combining intelligent algorithms to design a multifreedom structure.

To address the manufacturing tolerances of this reconfigurable Janus metasurface, we conducted simulations to assess the effects of varying the length, width, and thickness of the top Sb_2S_3 nanorods on the cross-polarized transmission spectrum, as depicted in Fig. 9. Figures 9(a)–9(c) illustrate the impact of different structural parameters including the width, length, and thickness of A-Sb_2S_3 nanorods on the efficiency of cross-polarization conversion. In each figure, the peak transmission offset is represented by a black dashed line. Furthermore, Figs. 9(d)–9(f) illustrate the impact of different width, length, and thickness of C-Sb_2S_3 nanorods on the efficiency of cross-polarization conversion. Figure 9 implies that the reconfigurable Janus metasurface can still maintain good performance within a certain range of structural size.

3. CONCLUSIONS

In summary, we demonstrated the use of a reconfigurable Janus metasurface based on single-sized nanostructures for dynamic switching displays without the need for complex and difficult manufacturing processes. In addition, we proposed a modified

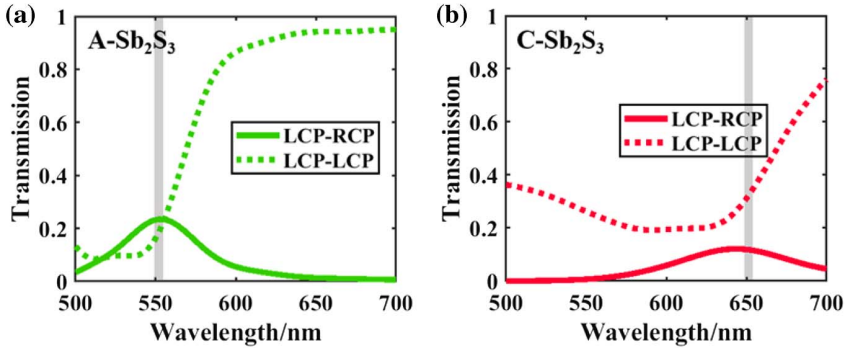

Fig. 7. Co-polarization and cross-polarization transmission efficiency of the reconfigurable Janus metasurface sample with different crystallinity. (a) A-Sb_2S_3. (b) C-Sb_2S_3.

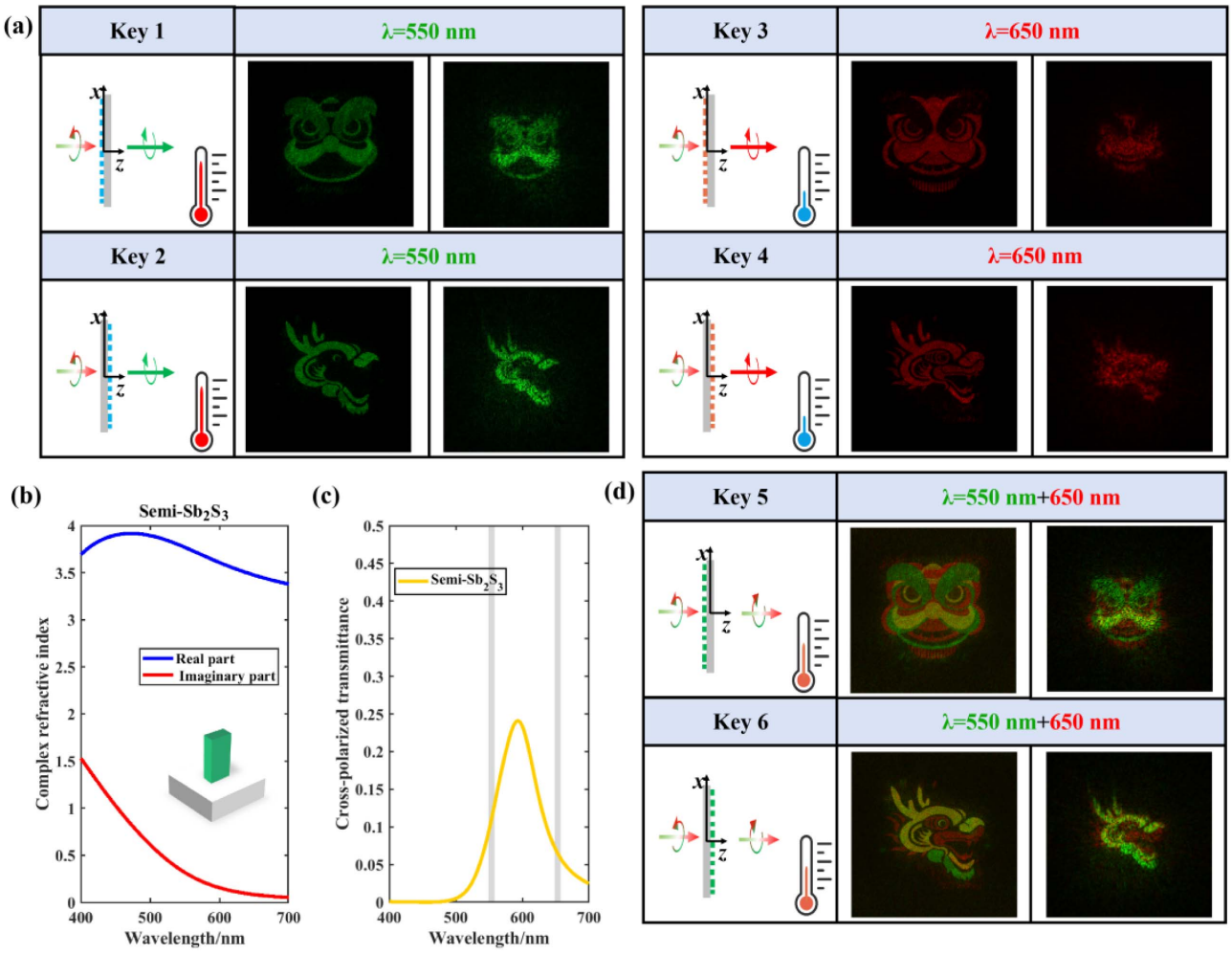

Fig. 8. (a) Simulation results of a single wavelength LCP incident light with a wavelength of 550 nm (650 nm) when the metasurface is in an amorphous (crystalline) state. (b) Complex refractive index curve of the semi-crystalline Sb_2S_3. (c) Cross-polarization conversion efficiency of meta-atoms in a semi-crystalline state. (d) Simulation results of dual-wavelength LCP incident light at 550 nm and 650 nm when the metasurface is in a semi-crystalline state.

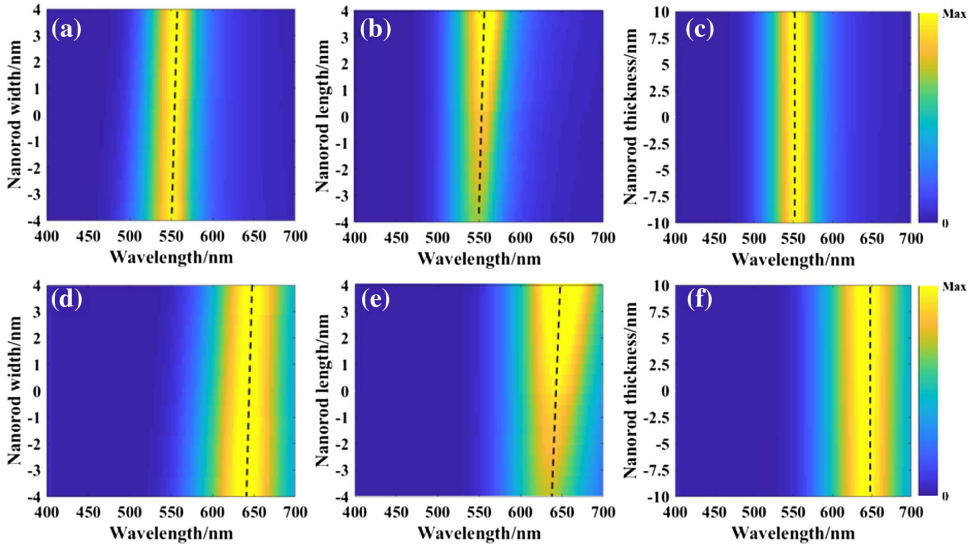

Fig. 9. Manufacturing tolerances of the reconfigurable Janus metasurface. (a) Variation of the simulated cross-polarization transmission spectra of A-Sb_2S_3 nanorods with different lengths, widths, and thicknesses. (b) Variation of the simulated cross-polarization transmission spectra of C-Sb_2S_3 nanorods with different lengths, widths, and thicknesses.

holographic optimization strategy to achieve high-fidelity asymmetric holographic imaging. The mechanism underlying this approach combines the geometric phase and crystallinity transitions, resulting in different optical responses to the same CP light when incident from opposite directions. In the visible region, we realized a color-holographic encryption display of wavelength, incident direction, and crystal state using an O-PCM array, which was previously impossible with asymmetric transmission metasurfaces. The results demonstrate that the display of different color holographic patterns can be independently controlled by switching three keys: wavelength, incident direction, and crystal state. Furthermore, by combining this scheme with deep learning methods or other optimization algorithms, the number of image channels encoded within a single metasurface can be further increased. With the advantages of miniaturization, integration, and tunability, reconfigurable metasurfaces hold significant potential for application in next-generation color-optical encryption elements.

APPENDIX A: PARAMETERS OF SELECTED NANOBRICKS

The transmittance of meta-atoms with varying sizes (L and W ranging from 50 to 160 nm) was simulated at different wavelengths, crystallinity, and polarization states by using FDTD solutions, as shown in Fig. 10. The solid circle represents the optimal size selected for the structure.

APPENDIX B

To achieve Sb_2S_3 nanorods with excellent narrowband filtering characteristics, the introduction of intelligent algorithms for optimal design is necessary. We utilized the particle swarm optimization algorithm to optimize the size of the structure, as depicted in Fig. 11. The length, width, and height of the Sb_2S_3 nanorod structure are primarily optimized here. The period, P, is fixed at 380 nm. First, a random function was utilized to generate a series of samples with varying sizes. The corresponding spectral characteristics were obtained by calculating the Maxwell equation and compared with the objective function of an ideal spectral curve. Then, the size of the other samples was gradually adjusted to approach the size of the optimal sample, refining the spectral characteristics and generating new samples. At each iteration, the performance of the optimal sample was evaluated to determine whether to continue or terminate the iteration. Consequently, the optimal sample reached the target performance, and the iteration was terminated after several rounds of optimization. Finally, the sample with the best performance was selected, and the designed structure was finalized. It is worth noting that we chose single-layer rectangular nanorods and further optimized the structural size for facilitating manufacturing. Due to the simple structure and the optical loss arising from the extinction coefficient of Sb_2S_3 nanorods, the polarization conversion efficiency of the metasurface is limited.

APPENDIX C

The versatile wave manipulation capabilities of asymmetric transmission metasurfaces make them highly attractive for applications in information encryption and storage. In recent years, significant research efforts have focused on enhancing the information processing capabilities of metasurface holograms through asymmetric transmission. Table 1 summarizes our work and provides a detailed comparison with other asymmetric transmission surfaces to highlight the unique properties of metasurfaces based on the nonvolatile O-PCM Sb_2S_3. The simple single-layer metasurface structure effectively reduces the manufacturing difficulty and cost compared to Refs. [28,47], which utilize high-precision and complex multilayer structures.

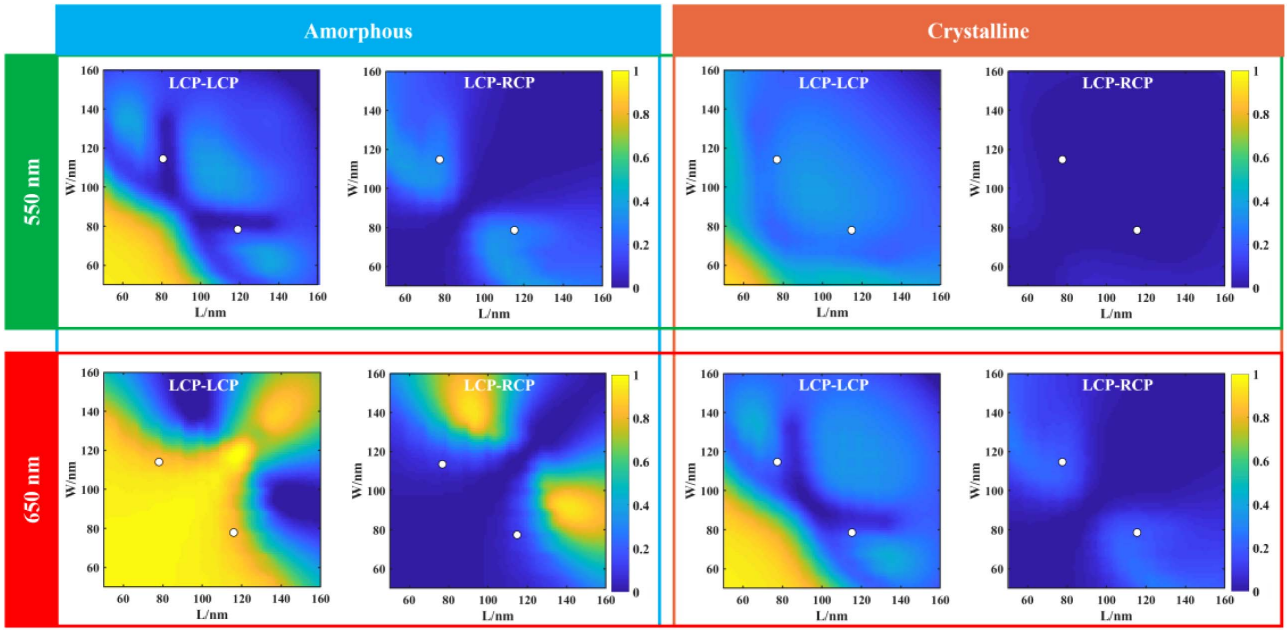

Fig. 10. Numerical analysis of unit structures for reconfigurable asymmetric transmittance metasurfaces. The scanning results are separately calculated for different wavelengths, levels of crystallinity, and polarization states.

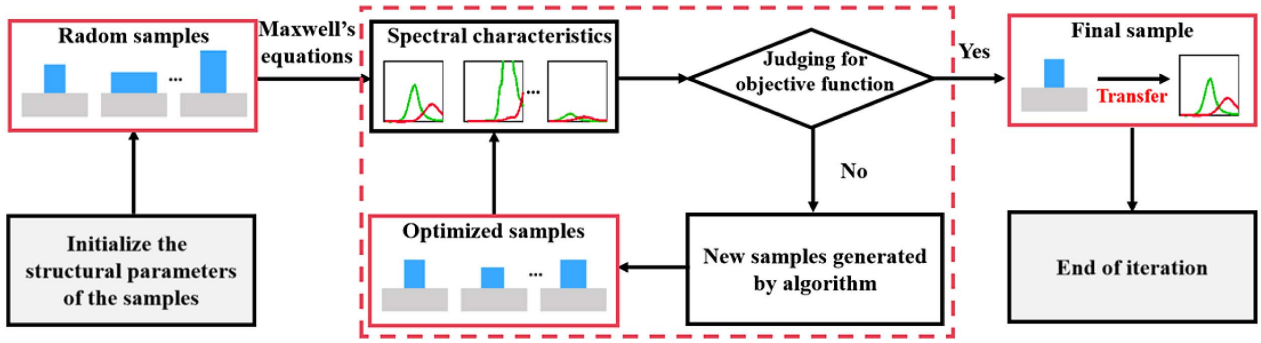

Fig. 11. Design process of the PSO algorithm for optimizing the size of the nanorods.

Table 1. Comparison between Our Work and Other Reported Works

Refs.	[28]	[32]	[34]	[47]	This work
Material	Cu, dielectric substrates	a-Si:H, SiO_2	a-Si, SiO_2	Au, polyimide, VO_2, Al_2O_3	Sb_2S_3, SiO_2
Target wavelength	8.6 GHz	632.8 nm	663 nm	0.99 THz	550 nm, 650 nm
Structure mode	Three layers cascade	Single layer	Single layer	Three layers cascade	Single layer
Asymmetric transmission	√	√	√	√	√
Reconfigurable	×	×	×	√	√
Nonvolatile	×	×	×	×	√
Decoding key	Direction of propagation	Direction of propagation	Direction of propagation	Direction of propagation, crystallinity	Direction of propagation, crystallinity, wavelength
Number of channels	2	2	2	4	6

The nonvolatile reconfigurable metasurface based on Sb_2S_3 can additionally perform dynamic switching of holographic images, effectively improving the information capacity. In contrast to the volatile VO_2-based metasurface, this metasurface is capable of maintaining a specific function without requiring additional stimulus. Compared to traditional asymmetric transmission metasurface described in Refs. [32,34], we have utilized Sb_2S_3 to achieve an asymmetric color holographic display in the visible light band for the first time. With this advantage, it is expected to achieve advanced applications such as dynamic bidirectional color display and encryption.

APPENDIX D

The potential manufacturing steps for the proposed reconfigurable Janus metasurface are depicted in Fig. 12. First, a 500 nm thick layer of Sb_2S_3 is deposited on a SiO_2 substrate using the plasma-enhanced chemical vapor deposition method. The photoresist is spin-coated and deposited onto the Sb_2S_3 layer, then exposed using an electron beam lithography system. Following this, the Cr masking layer is applied, and the stripping process is performed. The electron beam deposition method is then employed to deposit a layer of Cr and the photoresist is removed. Finally, the manufacturing process is completed by performing dry etching to remove the Cr layer.

APPENDIX E

To characterize the optical properties of our reconfigurable Janus metasurface, we proposed a holographic imaging device for the visible spectrum under CP light incident conditions, as shown in Fig. 13. Two lasers with respective wavelengths of

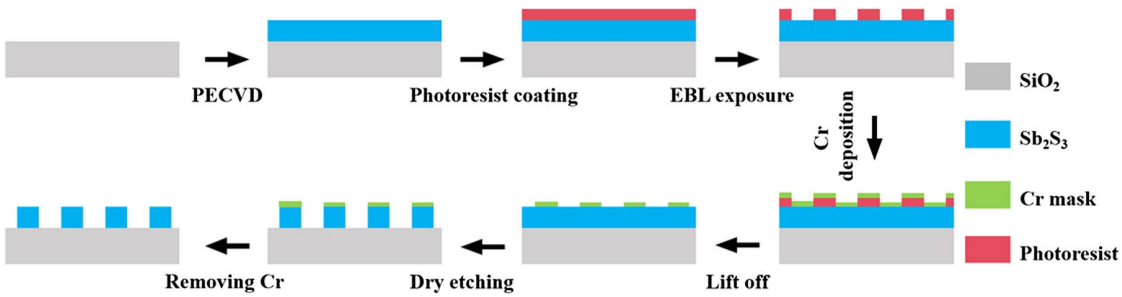

Fig. 12. Potential manufacturing steps for the reconfigurable Janus metasurface.

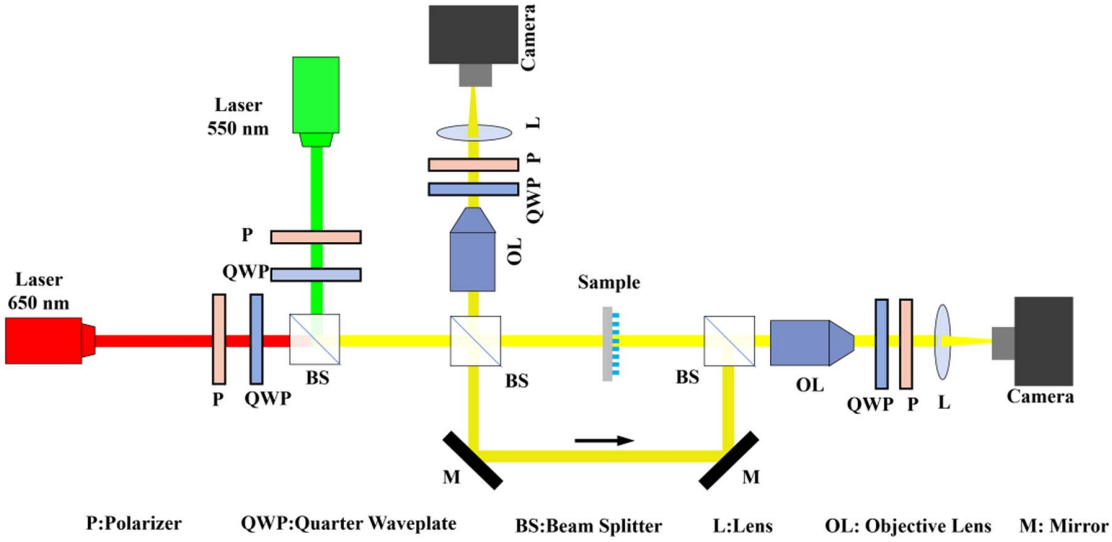

Fig. 13. Potential experimental setup for measuring the encrypted holographic images.

550 nm and 650 nm, act as the incident light sources. A combination of a polarizer (P) and a quarter-wave plate (QWP) is used to generate CP light. Beam splitters and mirrors are employed on both sides of the metasurface to achieve a consistent CP light source for both forward and backward incidence. The monitoring device utilizes two charge-coupled device cameras to capture images through an objective (OL), P, QWP, and lens on both sides. The OL mounted behind the metasurface is used for magnifying the holographic image.

Funding. National Natural Science Foundation of China (61905167); National Key Research and Development Program of China (2020YFA0714001).

Disclosures. The authors declare no conflicts of interest.

Data Availability. Data underlying the results presented in this paper are not publicly available at this time but may be obtained from the authors upon reasonable request.

REFERENCES

1. N. Yu, P. Genevet, M. A. Kats, *et al.*, "Light propagation with phase discontinuities: generalized laws of reflection and refraction," Science **334**, 333–337 (2011).
2. X. Chen, L. Huang, H. Mühlenbernd, *et al.*, "Dual-polarity plasmonic metalens for visible light," Nat. Commun. **3**, 1198 (2012).
3. A. V. Kildishev, A. Boltasseva, and V. M. Shalaev, "Planar photonics with metasurfaces," Science **339**, 1232009 (2013).
4. N. Yu and F. Capasso, "Flat optics with designer metasurfaces," Nat. Mater. **13**, 139–150 (2014).
5. M. Khorasaninejad, W. T. Chen, R. C. Devlin, *et al.*, "Metalenses at visible wavelengths: diffraction-limited focusing and subwavelength resolution imaging," Science **352**, 1190–1194 (2016).
6. L. Huang, X. Chen, H. Mühlenbernd, *et al.*, "Three-dimensional optical holography using a plasmonic metasurface," Nat. Commun. **4**, 2808 (2013).
7. D. Wen, F. Yue, G. Li, *et al.*, "Helicity multiplexed broadband metasurface holograms," Nat. Commun. **6**, 8241 (2015).
8. H. Ren, G. Briere, X. Fang, *et al.*, "Metasurface orbital angular momentum holography," Nat. Commun. **10**, 2986 (2019).
9. R. Zheng, R. Pan, G. Geng, *et al.*, "Active multiband varifocal metalenses based on orbital angular momentum division multiplexing," Nat. Commun. **13**, 4292 (2022).
10. P. Georgil, Q. Wei, B. Sain, *et al.*, "Optical secret sharing with cascaded metasurface holography," Sci. Adv. **7**, eabf9718 (2021).
11. G. Qu, W. Yang, Q. Song, *et al.*, "Reprogrammable meta-hologram for optical encryption," Nat. Commun. **11**, 5484 (2020).
12. I. Kim, J. Jang, G. Kim, *et al.*, "Pixelated bifunctional metasurface-driven dynamic vectorial holographic color prints for photonic security platform," Nat. Commun. **12**, 3614 (2021).
13. X. Guo, P. Li, J. Zhong, *et al.*, "Stokes meta-hologram toward optical cryptography," Nat. Commun. **13**, 6687 (2022).
14. H. Yang, P. He, K. Ou, *et al.*, "Angular momentum holography via a minimalist metasurface for optical nested encryption," Light Sci. Appl. **12**, 79 (2023).
15. F. Zhang, Y. Guo, M. Pu, *et al.*, "Meta-optics empowered vector visual cryptography for high security and rapid decryption," Nat. Commun. **14**, 1946 (2023).
16. X. M. Goh, Y. Zheng, S. J. Tan, *et al.*, "Three-dimensional plasmonic stereoscopic prints in full colour," Nat. Commun. **5**, 5361 (2014).
17. S. J. Tan, L. Zhang, D. Zhu, *et al.*, "Plasmonic color palettes for photorealistic printing with aluminum nanostructures," Nano Lett. **14**, 4023–4029 (2014).
18. J. Deng, L. Deng, Z. Guan, *et al.*, "Multiplexed anticounterfeiting meta-image displays with single-sized nanostructures," Nano Lett. **20**, 1830–1838 (2020).
19. Y. Cao, L. Tang, J. Li, *et al.*, "Four-channel display and encryption by near-field reflection on nanoprinting metasurface," Nanophotonics **11**, 3365–3374 (2022).
20. J. Deng, Z. Li, J. Li, *et al.*, "Metasurface-assisted optical encryption carrying camouflaged information," Adv. Opt. Mater. **10**, 2200949 (2022).
21. Y. Zhang, P. Lin, P. Huo, *et al.*, "Dielectric metasurface for synchronously spiral phase contrast and bright-field imaging," Nano Lett. **23**, 2991–2997 (2023).
22. B. Song, S. Wen, and W. Shu, "Topological differential microscopy based on the spin–orbit interaction of light in a natural crystal," ACS Photonics **9**, 3987–3994 (2022).
23. G. Ma, J. Yu, R. Zhu, *et al.*, "Optical multi-imaging-casting accelerator for fully parallel universal convolution computing," Photonics Res. **11**, 299–312 (2023).
24. H. Zhou, J. Dong, J. Cheng, *et al.*, "Photonic matrix multiplication lights up photonic accelerator and beyond," Light Sci. Appl. **11**, 30 (2022).

25. C. Qian, B. Zheng, Y. Shen, *et al.*, "Deep-learning-enabled self-adaptive microwave cloak without human intervention," Nat. Photonics **14**, 383–390 (2020).
26. Z. L. Deng, M. Jin, X. Ye, *et al.*, "Full-color complex-amplitude vectorial holograms based on multi-freedom metasurfaces," Adv. Funct. Mater. **30**, 1910610 (2020).
27. Y. Ni, C. Chen, S. Wen, *et al.*, "Computational spectropolarimetry with a tunable liquid crystal metasurface," eLight **2**, 23 (2022).
28. K. Chen, G. Ding, G. Hu, *et al.*, "Directional Janus metasurface," Adv. Mater. **32**, 1906352 (2019).
29. K. Chen and Y. Feng, "A review of recent progress on directional metasurfaces: concept, design, and application," J. Phys. D **55**, 383001 (2022).
30. V. A. Fedotov, P. L. Mladyonov, S. L. Prosvirnin, *et al.*, "Asymmetric propagation of electromagnetic waves through a planar chiral structure," Phys. Rev. Lett. **97**, 167401 (2006).
31. C. Menzel, C. Helgert, C. Rockstuhl, *et al.*, "Asymmetric transmission of linearly polarized light at optical metamaterials," Phys. Rev. Lett. **104**, 253902 (2010).
32. M. A. Naveed, M. A. Ansari, I. Kim, *et al.*, "Optical spin-symmetry breaking for high-efficiency directional helicity-multiplexed metaholograms," Microsyst. Nanoeng. **7**, 5 (2021).
33. C. Wan, C. Dai, S. Wan, *et al.*, "Dual-encryption freedom via a monolayer-nanotextured Janus metasurface in the broadband visible," Opt. Express **29**, 33954–33961 (2021).
34. X. Liang, L. Deng, X. Shan, *et al.*, "Asymmetric hologram with a single-size nanostructured metasurface," Opt. Express **29**, 19964–19974 (2021).
35. M. A. Ansari, I. Kim, I. D. Rukhlenko, *et al.*, "Engineering spin and antiferromagnetic resonances to realize an efficient direction-multiplexed visible meta-hologram," Nanoscale Horiz. **5**, 57–64 (2020).
36. Y. Zhang, J. B. Chou, J. Li, *et al.*, "Broadband transparent optical phase change materials for high-performance nonvolatile photonics," Nat. Commun. **10**, 4279 (2019).
37. Q. Zhang, Y. Zhang, J. Li, *et al.*, "Broadband nonvolatile photonic switching based on optical phase change materials: beyond the classical figure-of-merit," Opt. Lett. **43**, 94–97 (2018).
38. M. Delaney, I. Zeimpekis, D. Lawson, *et al.*, "A new family of ultralow loss reversible phase-change materials for photonic integrated circuits: Sb_2S_3 and Sb_2Se_3," Adv. Funct. Mater. **30**, 2002447 (2020).
39. M. Wang, J. S. Lee, S. Aggarwal, *et al.*, "Varifocal metalens using tunable and ultralow-loss dielectrics," Adv. Sci. **10**, 2204899 (2023).
40. C. Choi, S. Mun, J. Sung, *et al.*, "Hybrid state engineering of phase-change metasurface for all-optical cryptography," Adv. Funct. Mater. **31**, 2007210 (2021).
41. F. Zhang, X. Xie, M. Pu, *et al.*, "Multistate switching of photonic angular momentum coupling in phase-change metadevices," Adv. Mater. **32**, 1908194 (2020).
42. G. Chen, J. Zhou, S. E. Bopp, *et al.*, "Visible and near-infrared dual band switchable metasurface edge imaging," Opt. Lett. **47**, 4040–4043 (2022).
43. M. Delaney, I. Zeimpekis, H. Du, *et al.*, "Nonvolatile programmable silicon photonics using an ultralow-loss Sb_2Se_3 phase change material," Sci. Adv. **7**, eabg3500 (2021).
44. J. Zheng, Z. Fang, C. Wu, *et al.*, "Nonvolatile electrically reconfigurable integrated photonic switch enabled by a silicon PIN diode heater," Adv. Mater. **32**, 2001218 (2020).
45. S. Raoux, F. Xiong, M. Wuttig, *et al.*, "Phase change materials and phase change memory," MRS Bull. **39**, 703–710 (2014).
46. O. Hemmatyar, S. Abdollahramezani, I. Zeimpekis, *et al.*, "Advanced phase-change materials for enhanced meta-displays," arXiv, arXiv:2105.01313 (2021).
47. B. Chen, S. Yang, J. Chen, *et al.*, "Directional terahertz holography with thermally active Janus metasurface," Light Sci. Appl. **12**, 136 (2023).
48. D. Zhang, G. Pan, Z. Jin, *et al.*, "Tunable dielectric metasurfaces by structuring the phase-change material," Opt. Express **30**, 4312–4326 (2022).